Journal of Materials Chemistry A

Ultrathin Microporous Metal-Organic Network Membranes for Molecular Separation

Journal:	*Journal of Materials Chemistry A*
Manuscript ID	TA-ART-09-2021-007883.R1
Article Type:	Paper
Date Submitted by the Author:	28-Oct-2021
Complete List of Authors:	Zhang, Shenxiang; Soochow University Ciora, Richard ; Rensselaer Polytechnic Institute Sengupta, Bratin ; Rensselaer Polytechnic Institute Li, Huazheng; University at Buffalo, Chemical and Biological Engineering Belfort, Georges; Rensselaer Polytechnic Institute, Howard P, Isermann Department of Chemical and Biological Engineering Li, Shiguang; Gas Technology Institute Zhou, Rongfei; Nanjing Tech University Yu, Miao; University at Buffalo, Chemical and Biological Engineering

ARTICLE

Ultrathin Microporous Metal-Organic Network Membranes for Molecular Separation

Received 00th January 20xx,
Accepted 00th January 20xx

DOI: 10.1039/x0xx00000x

Shenxiang Zhang[a,b], Richard Ciora[b,c], Bratin Sengupta[b,c], Huazheng Li[b,c], Georges Belfort[b], Shiguang Li[d], Rongfei Zhou[e], and Miao Yu*[b,c]

Microporous materials are ideal building blocks for separation membranes due to their molecular-sized pores and high porosity. However, it is challenging to assemble/grow crystalline microporous materials, such as zeolites, metal-organic frameworks (MOFs), and covalent organic frameworks (COFs), into ultrathin and defect-free selective membranes. Amorphous microporous materials, such as polymers of intrinsic microporosity (PIMs), have been deposited as ultrathin selective membranes, but their chemical stability, especially in various organic solvents, may be a concern. Herein, for the first time we report microporous metal-organic networks (mMONs) formed *via* alcoholysis reaction between contorted/rigid organic units with catechol groups and metal linkers. mMONs exhibit similar microporosity to existing microporous materials, high chemical stability and structural integrity against various chemical environments, because of the contortion and rigidity of the organic units and covalent bonds between metal linkers and catechol groups. An interfacial process is developed to fabricate ultrathin mMON membrane (30-120 nm). Compared with the reported organic solvent nanofiltration (OSN) membranes with similar molecular weight cut-off (MWCO), mMON membranes exhibit similar or higher solvent permeanc.

Introduction

Membrane separation is gaining continuous attention in chemical, petrochemical, energy and environment-related industries due to its high separation efficiency, absence of a phase-change, low operating cost, and process simplicity.[1-4] To further boost membrane separation efficiency, it is vital to design and synthesize novel membrane materials and develop viable ways to assemble/fabricate them into defect-free nanofilms with both high selectivity and high permeance.[5-7] An ideal permselective membrane is expected to have high-density molecular-sized pores and an ultrathin active separation layer for highly selective and low-resistance permeation.[8-12] In addition, high chemical stability is also required, considering separation in harsh chemical environments.[13-15]

Microporous crystalline materials with uniform molecular-sized pores, such as zeolites[16-18], metal-organic frameworks (MOFs)[19-21], and covalent organic frameworks (COFs)[22-25], are excellent candidates for highly permeable and selective membranes. However, it is challenging to assemble/grow these crystalline materials into ultrathin (<100 nm), defect-free, selective membranes because of the presence of defects and unavoidable grain boundaries.[26-31] Recently, novel synthesis strategies[32] and 2-dimensional crystalline materials[7,33] have shown potential for making ultrathin membranes from MOFs and zeolites. For amorphous microporous materials, polymers of intrinsic microporosity (PIMs) is a notable example, which are synthesized from contorted, rigid monomers.[6,34-36] Because of the inefficient packing of polymer chains, PIM materials are endowed with high free volume, resulting in high permeability (=permeance × membrane thickness) of gases.[37-39] To achieve high permeance, PIMs have also been used to form ultrathin selective membranes.[40] However, thinner PIM membranes do not necessarily have higher permeance, due to the structural relaxation of polymer chains in the ultrathin membrane.[40] Moreover, solubility of PIMs in a range of polar solvents also restricted their wide applications in organic solvent nanofiltration (OSN).[41,42] One promising strategy addressing this issue is to form a crosslinked, rigid nanofilm *via* interfacial polymerization.[43-46] In addition, amorphous carbon was deposited as an ultrathin membrane by chemical vapor deposition, which was shown to be mechanically robust and exhibited high OSN separation performance.[9] These pioneering publications on fabricating membranes composed of microporous materials, especially those with ultrathin

[a] *College of Chemistry, Chemical Engineering and Materials Science, Soochow University, Suzhou 215123, P.R. China.*
[b] *Department of Chemical and Biological Engineering, Rensselaer Polytechnic Institute, Troy, NY 12180, USA. E-mail: myu9@buffalo.edu*
[c] *Department of Chemical and Biological Engineering and RENEW Institute, University at Buffalo, Buffalo, NY 14260, USA.*
[d] *Gas Technology Institute, 1700 South Mount Prospect Road, Des Plaines, IL 60018, USA.*
[e] *State Key Laboratory of Materials-Oriented Chemical Engineering, College of Chemical Engineering, Nanjing Tech University, Nanjing 210009, P. R. China*
† Electronic Supplementary Information (ESI) available: Additional characterization data. See DOI: 10.1039/x0xx00000x

thickness, have encouraged material and membrane scientists to further expand the microporous materials family and develop novel and compatible methods for membrane fabrication.

In this work, we report, for the first time, microporous metal-organic networks (mMONs), formed via covalent bonds between contorted/rigid organic units with catechol groups and metal linkers. mMONs demonstrate similar microporosity to the existing microporous materials and show high chemical stability and excellent structure integrity against various chemical environments. Furthermore, we develop an interfacial process to deposit ultrathin, defect-free mMON nanofilms/membranes with adjustable pore size and thickness down to ~30 nm and demonstrate their OSN performance.

Experimental

Synthesis of mMON particles.

mMON particles were prepared by monophasic reactions. Two organic units, 5,5',6,6'-tetrahydroxy-3,3,3',3'-tetramethylspirobisindane (TTSBI, Sigma-Aldrich) and 2,3,6,7,10,11-hexahydroxytriphenylene (HHTP, TCI), and three metal alkoxide precursors, titanium(IV) butoxide ($Ti(OBu)_4$, Sigma-Aldrich), zirconium(IV) butoxide ($Zr(OBu)_4$, Sigma-Aldrich), and tin(IV) tert-butoxide ($Sn(t\text{-}OBu)_4$, Sigma-Aldrich), were used. For TTSBI-Ti/Zr/Sn particles synthesis, 1.0 mmol TTSBI was dissolved in 20 mL anhydrous acetone. A solution of 0.6 mmol metal alkoxide precursors ($Ti(OBu)_4$ for TTSBI-Ti, $Zr(OBu)_4$ for TTSBI-Zr, and $Sn(t\text{-}OBu)_4$ for TTSBI-Sn) in 20 mL anhydrous acetone was slowly added into the TTSBI solution with stirring under nitrogen atmosphere. After reaction at 23 °C for 30 min, precipitates were formed, which were washed with acetone, methanol and hexane, respectively. The precipitates were dried at 60 °C in a forced air oven for 2 h, and then at 100 °C in a vacuum oven for 12 h. For HHTP-Ti/Zr/Sn synthesis, 1.0 mmol HHTP was dissolved in 20 mL anhydrous N-methyl-2-pyrrolidone (NMP). A solution of 1.0 mmol metal alkoxide precursors, ($Ti(OBu)_4$ for HHTP-Ti, $Zr(OBu)_4$ for HHTP-Zr, and $Sn(t\text{-}OBu)_4$ for HHTP-Sn), in 20 mL anhydrous acetone was slowly added into the HHTP solution with stirring under nitrogen atmosphere. After reaction at 23 °C for 30 min, precipitates were formed, which were washed with NMP, methanol and hexane, respectively. The precipitates were dried at 60 °C in a forced air oven for 2 h, and then at 100 °C in a vacuum oven for 12 h.

Synthesis of freestanding mMON nanofilms.

Freestanding mMON nanofilms were synthesized by interfacial reaction. The organic precursors, TTSBI or HHTP were dissolved in anhydrous NMP with the concentrations of 20 mM. A solution of 10 mM $Ti(OBu)_4$ in tetradecane was slowly added to the top of NMP solution, and allowed to react for 2 min. The nanofilms were immediately withdrawn from the interface with a clean glass substrate, washed in hexane and methanol, and then transferred to an anodized aluminum oxide support (AAO, Whatman) with a surface layer of 150-200 nm pores.

Fabrication of AAO supported carbon nanotube (CNT) network.

10 mg single-walled CNT powder (OD: <3 nm; length: 5 μm; purity: >85%; TCI) was dispersed in 100 mL 1.0 mg mL^{-1} sodium dodecylbenzene sulfonate (SDBS) solution using an ultrasonic cell crusher (QSonica Q500) under 10 W of power for 1 h. Then, the as-prepared CNT dispersion was centrifuged at 8,000 rpm for 30 min, and the supernatant dispersion was collected with the concentration of ~0.06 mg mL^{-1}. The CNT network was prepared through vacuum filtering a 10.0-ml 0.001 mg/mL CNT dispersion onto an AAO support with diameter of 25 mm and pore size of 150-200 nm. After vacuum filtration, the CNT network substrate was dried in a forced air oven at 80 °C for 12 h.

Synthesis of CNT network/AAO supported mMON membranes.

The supported mMON membranes were synthesized by interfacial reaction at 23 °C. In detail, a swatch of CNT network/AAO support was placed onto a glass plate where 0.5 ml of NMP solution containing organic units, TTSBI or HHTP, was preloaded. To make sure CNT network was fully wetted, another 0.5 mL organic unit solution was dropped onto the surface and stood for 30 s. The excess solution was removed by dry nitrogen purging until no obvious solution spot can be observed on the surface. 1.0 ml tetradecane containing certain amount of $Ti(OBu)_4$ was then dropped onto the above pre-wetted membrane surface and stood for 2 min. After removing the excess $Ti(OBu)_4$ solution, the membrane was immersed into hexane and methanol, respectively, to remove unreacted precursors and then dried in a forced air oven at 80 °C for 30 min to obtain CNT network/AAO supported mMON membranes. As for the supported mMON membranes with different thickness, different concentrations of organic unit solution (20 – 160 mM) and $Ti(OBu)_4$ solutions (10 – 80 mM) were used.

Characterization methods.

Scanning electron microscopy (SEM) images were taken from a FEI Veras scanning electron microscope. Transmission electron microscopy (TEM) images were acquired from a JEOL JEM-2011 200KV field-emission transmission electron microscope. X-ray photoelectron spectroscopy (XPS) spectra were taken from a Physical Electronics Versa Probe X-ray photoelectron spectrometer system. Fourier transform infrared (FTIR) spectra in the range of 4,000-400 cm^{-1} were measured using a Thermo Scientific Nicolet iS5 Fourier transform infrared spectroscopy. Ultraviolet-visible (UV-vis) spectra were acquired from Thermo Scientific GENESYS spectrophotometer. Wide-angle X-ray diffraction (XRD) patterns were measured using a Bruker D8-Discover powder X-Ray diffractometer using CuK radiation. Small-angle x-ray scattering (SAXS) measurements were carried out on a Bruker Nanostar-U instrument. Thermogravimetric analysis (TGA) was performed with a TA Instruments TGA-Q50. mMON particles were heated from room temperature to 600 °C with heating rate as 10 °C min^{-1} in nitrogen and air atmosphere. The porous properties of mMON

samples were determined *via* nitrogen physisorption at 77 K by using a Micromeritics 3Flex physisorption analyzer. Before the measurement, samples were evacuated at 200 °C for 3 h. The specific surface areas were calculated in the pressure range from 0.05 to 0.35 using multipoint Brunauer-Emmett-Teller (BET) method. Microporous pore size distribution and volume were determined from adsorption branch by using Horvath-Kawazoe model. Microporous surface area was calculated by t-plot. BET surface area usually corresponds to total surface area (= micropore surface area + mesopore and external area, based on t-plot).

OSN performance test.

OSN performance was evaluated in terms of permeance of organic solvent and rejection of representative dye molecules with varied molecular weights. The OSN experiments were carried out in a dead-end stirred cell (350 r.p.m.) at 23 °C and 5.0-6.0 bar (absolute pressure). mMON membrane supported by CNT network/AAO was fixed in a filtration cell with separation area of 28.3 mm^2. For this OSN experiments, azobenzene (AZ), methyl orange (MO), crystal violet (CV), indigo carmine (IC) and brilliant blue R (BB) with a concentration of 100 mg L^{-1} were dissolved in methanol, respectively. 40 mL feed solution was filled in the feed cell, and ~5 mL permeate solution was collected in each OSN experiment. A fresh membrane was used for each permeation and rejection measurement. The concentration of the dye at the feed and permeate side was measured by UV-vis absorption. Solvent permeance (J, L m^{-2} h^{-1} bar^{-1}) was calculated by the following equation: $J = V/(A \times t \times \Delta P)$, where V is permeate volume (L), A is effective membrane area (m^2), t is time (h), and ΔP is applied pressure (bar). The rejection (R_i) of dye was calculated from $R_i = (1 - (C_{P,i}/C_{F,i})) \times 100\%$, where $C_{P,i}$ and $C_{F,i}$ correspond to dye concentrations at the permeate and the feed, respectively.

Results and discussion

Formation mechanism and characterization of mMONs

Our strategy of introducing microporosity in mMONs involved alcoholysis reaction of metal alkoxides with catechol-based organic units (see proposed reaction scheme in Fig. S1). We used two types of catechol building units: spiro-structured TTSBI, and planar-structured HHTP (Fig. 1a). Three metal alkoxide precursors, including $Ti(OBu)_4$, $Zr(OBu)_4$, and $Sn(t\text{-}OBu)_4$, were used (Fig. 1a). Via the combination of two organic units and three metal precursors, six different mMONs, TTSBI-Ti (organic unit: TTSBI; metal linker: Ti. Similar abbreviation was used below), TTSBI-Zr, TTSBI-Sn, HHTP-Ti, HHTP-Zr, and HHTP-Sn, respectively, were synthesized. The spiro centers in TTSBI units possess a dihedral angle of 90°. Therefore, when they reacted with metal alkoxides, the TTSBI units formed contorted structures in mMONs (Fig. 1b), which inhibited the efficient packing of chains in the network, leading to molecular-sized pores and relatively high porosity. Planar HHTP molecule also has a rigid structure and three catechol groups, therefore reaction between HHTP and metal alkoxides also generated a microporous structure (Fig. 1c). mMON particles can be synthesized by homogeneous liquid phase reaction between organic units and metal linkers, as described in Method. SEM image (Fig. 2a) shows that TTSBI-Ti has a particle size of 40-500 nm and irregular shape. Transmission electron microscope (TEM) image and selected area electron diffraction pattern in Fig. 2b demonstrate the amorphous nature of TTSBI-Ti. XRD patterns (Fig. S2) further confirmed amorphous nature of TTSBI-Ti. After replacing Ti with Zr and Sn, smaller particle size of TTSBI-Zr and TTSBI-Sn were found (Fig. S3), probably because of different alcoholysis reaction and growth rate.

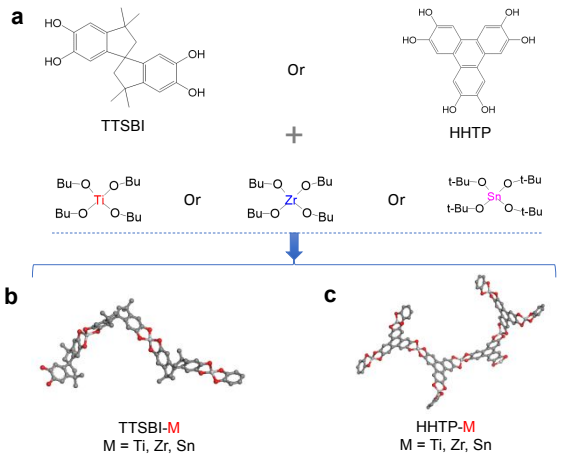

Fig. 1 Construction of mMONs. **a**, Formation mechanism of mMONs. Two representative organic units with contorted and rigid structures are shown: TTSBI and HHTP. Three metal precursors are used as linkers: Ti(OBu)4, Zr(OBu)4 and Sn(t-OBu)4. **b** and **c**, Molecular models of a segment of TTSBI-M and HHTP-M (M = Ti, Zr, Sn), respectively. C atom, gray; O atom, red; Ti atom, light gray.

The porous structure of TTSBI-Ti, TTSBI-Zr and TTSBI-Sn was characterized by N_2 adsorption at 77 K. All three materials exhibited a sharp increase at low relative pressure (P/P_0 <0.05) and then a platform (Fig. S4) characteristic of type I isotherms, indicating microporous structure. N_2 adsorbed amount continued to increase at higher relative pressure, suggesting multilayer adsorption and existence of mesopores. The mesopores appear to result from the packing of small particles (as shown in Fig. 2a) and may depend on the particle

Tab. 1. Surface area and pore volume of mMONs.

Sample	Surface area (m^2/g)		Micropore volume[c] (cm^3/g)
	BET[a]	*Micropore*[b]	
TTSBI-Ti	582	197	0.265
TTSBI-Zr	438	128	0.197
TTSBI-Sn	310	113	0.142
HHTP-Ti	572	192	0.259
HHTP-Zr	302	130	0.139
HHTP-Sn	160	68	0.098

[a] BET surface area calculated from N_2 adsorption isotherm at 77K.
[b] Micropore surface area calculated from t-Plot.
[c] Micropore volume calculated from N_2 adsorption isotherm using Horvath-Kawazoe equation.

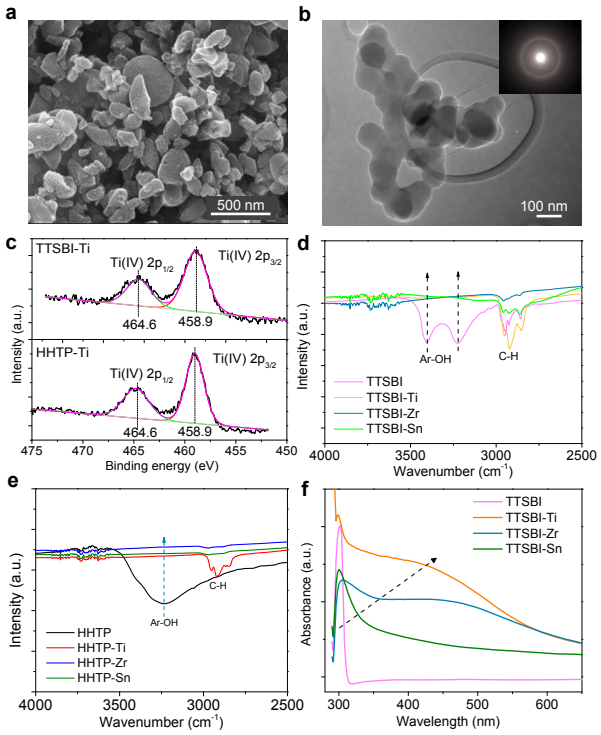

Fig. 2 Characterization of mMONs. **a**, SEM image of TTSBI-Ti particles prepared by monophasic reaction. **b**, TEM image of a TTSBI-Ti particle. The inset shows a selected area electron diffraction pattern indicating amorphous nature of TTSBI-Ti. **c**, Ti 2p XPS spectra of TTSBI-Ti and HHTP-Ti particles (black line: experimental spectrum; pink line: fitted spectrum; gray line: background). **d**, FTIR spectra of TTSBI and TTSBI-Ti/Zr/Sn mMONs. **e**, FTIR spectra of HHTP and HHTP-Ti/Zr/Sn mMONs. **f**, Ultraviolet-visible absorbance spectra of TTSBI and TTSBI-Ti/Zr/Sn mMONs.

size/shape and packing efficiency. To elucidate the intrinsic microporous properties of mMON materials, we summarized surface area and pore volume of micropores in Tab. 1; both BET surface area and micropore surface area are shown for reference. With increasing atomic weight of the metal linkers, micropore surface area and micropore volume of TTSBI-Ti, TTSBI-Zr and TTSBI-Sn decreased. However, the mMONs exhibited micropores with very similar size distributions and pore diameters centered at approximately 0.5 nm (Fig. S4). This suggests similar molecular structure of the mMONs and variation of pore volume and micropore surface area may result from the different atomic weights of metal linkers. When organic unit was changed to HHTP, HHTP-Ti, HHTP-Zr, and HHTP-Sn showed particle size of 20-100 nm (see SEM images in Fig. S5). They also exhibited type I isotherm at low relative pressure (P/P_0 <0.05), indicating microporous structure (Fig. S6). It is interesting that TTSBI-Ti and HHTP-Ti, TTSBI-Zr and HHTP-Zr presented the similar microporous surface area. We speculate that units formed by catechol group and metal linker determine the spatial configuration of microporous structure.

To demonstrate the critical role of the contorted/rigid organic units on generating microporosity, they were replaced by a small flexible organic molecule, ethylene glycol (EG). N_2 adsorption isotherm at 77K for EG-Ti showed negligible adsorbed amounts at relative pressure of P/P_0 <0.05, with BET surface area as low as 26.3 m^2/g and microporous area 2.8 m^2/g (Fig. S7). This supports our hypothesis that contorted/rigid organic units are essential for forming metal-organic networks with microporosity.

The theoretical molar ratio of organic units to metal linkers is 1:1 for TTSBI-Ti/Zr/Sn and 1:1.5 for HHTP-Ti/Zr/Sn, respectively. The mass fraction of metal linkers in mMONs was measured by TGA in air atmosphere (Fig. S8), assuming final residual at >550 °C will be metal oxides. The corresponding molar ratio of organic units to metal linkers was calculated to be 1:0.83 for TTSBI-Ti, 1:0.68 for TTSBI-Zr, 1:0.79 for TTSBI-Sn, 1:1.15 for HHTP-Ti, 1:1.28 for HHTP-Zr, and 1:1.00 for TTSBI-Sn, respectively. Apparently, metal linkers were insufficient in all six mMONs, suggesting some catechol groups were likely sequestered/tangled together and thus not available for reaction with metal linkers. To achieve the theoretical ratio and thus obtain a more open microporous structure, the reaction condition and synthesis procedure may need to be further optimized.

The surface chemistry of TTSBI-Ti and HHTP-Ti was studied by XPS. The survey spectra showed major peaks of carbon, oxygen and titanium in TTSBI-Ti and HHTP-Ti (Fig. S9). The high-resolution XPS spectra of the Ti(2p) (Fig. 2c) exhibited two energy bands at 458.9 and 464.6 eV, respectively, which are typical values of the Ti $2p_{2/3}$ and Ti $2p_{1/3}$ electrons of Ti^{4+}.[47] Fig. 2d shows the FTIR spectra of TTSBI and TTSBI-Ti/Zr/Sn. FTIR spectra displayed adsorption peaks in the range of 2,955-2,845 cm^{-1}, corresponding to asymmetric and symmetric vibration modes of the C-H bonds in TTSBI units. It is noteworthy that the significant peak intensity decrease was observed at 3,400 and 3,220 cm^{-1} (referring to O-H vibrational peaks of TTSBI). In HHTP-Ti/Zr/Sn samples, O-H vibrational peaks at 3,300 cm^{-1} also disappeared (Fig. 2e), indicating high conversion of O-H to O-M (M = Ti/Zr/Sn). Fig. 2f shows the UV–vis spectra of TTSBI and TTSBI-Ti/Zr/Sn. Compared with the UV–vis spectrum of TTSBI, TTSBI-Ti and TTSBI-Zr samples exhibited significant broadening and red shift for the original peak at 300 nm. The broader absorption band should be induced by metal- linked organic aromatic rings, which enlarge the π-electron delocalization in the conjugated system, indicating the formation of Ti-O bond between organic units and Ti linkers.

SAXS was used to investigate the pore architecture of mMONs. For TTSBI-Ti, a broad scattering peak can be observed in the range of $3.5 < q < 12$ nm^{-1}, indicating the distance between molecular chains was 0.52 - 1.79 nm (Fig. 3a). For HHTP-Ti, a broader scattering peak at $3.5 < q < 14$ nm^{-1} can be

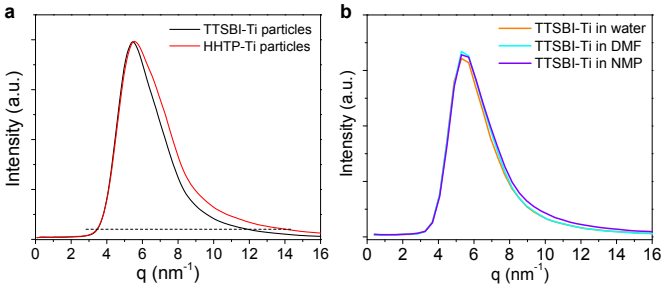

Fig. 3 a, SAXS patterns of TTSBI-Ti particles and HHTP-Ti particles. **b**, SAXS patterns of TTSBI-Ti particles dispersed in water, DMF, and NMP, respectively.

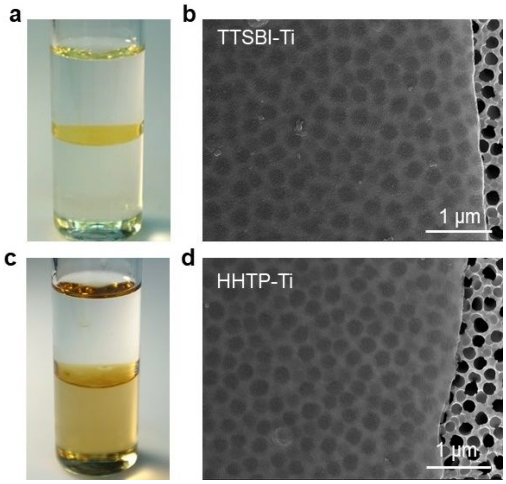

Fig. 4 Interfacial synthesis of mMON nanofilms. **a**, Photograph of a glass vial containing two immiscible solutions: TTSBI (20 mM) in NMP (bottom) and $Ti(OBu)_4$ (10 mM) in tetradecane (top). A TTSBI-Ti nanofilm is formed between the two phases by interfacial reaction. **b**, SEM image of TTSBI-Ti nanofilm supported on porous AAO. **c**, Photograph of a glass vial containing two immiscible solutions: HHTP (20 mM) in NMP (bottom) and $Ti(OBu)_4$ (10 mM) in tetradecane (top). **d**, SEM image of HHTP-Ti nanofilm supported on porous AAO.

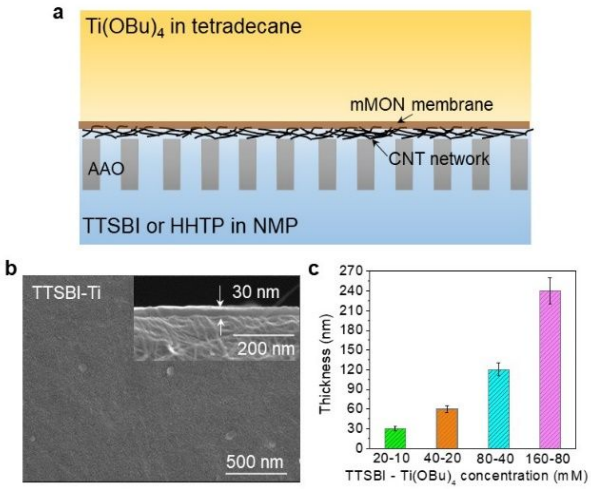

Fig. 5 Interfacial synthesis of mMON membranes. **a**, Schematic of mMON membrane formation on CNT network/AAO substrate. **b** Surface and cross-sectional SEM images of TTSBI-Ti membrane prepared by interfacial reaction between $Ti(OBu)_4$ (10 mM) in tetradecane and TTSBI (20 mM) in NMP. **c**, Thickness of TTSBI-Ti membrane *versus* precursor concentrations.

found (Fig. 3a), corresponding to distance of 0.45 - 1.79 nm between molecular chains.

To evaluate the chemical stability of mMONs, they were exposed to different chemical environments. TTSBI-Ti/Zr/Sn and HHTP-Ti/Zr/Sn particles were soaked in acid solutions and polar solvents at room temperature for 3 days. Fig. S10 shows that all mMON particles were stable and were not dissolved in 1 M HCl, NMP, and chloroform. In-situ SAXS characterization was also conducted to further confirm the structure integrity. Fig. 3b shows the peak position in their SAXS patterns didn't alter after being soaked in water, N,N-dimethylformamide (DMF), and NMP, suggesting TTSBI-Ti maintained its original skeleton and porous structure. Moreover, after being soaked in boiling water at 1 bar for 1 day, N_2 adsorption isotherm of TTSBI-Ti at 77 K was almost the same as that of the as-synthesized material (Fig. S11). Tab. S1 shows that after being soaked in 1 M HCl solution and in NMP solvent for 3 days, TTSBI-Ti particles maintained similar surface area and micropore volume, further confirming the preserved porosity. These results suggest the chemical bonds formed between catechol groups and metal linkers are strong and thus greatly improve the chemical stability of mMONs.

Interfacial synthesis of mMON nanofilms/membranes

We developed an interfacial synthesis process to fabricate ultrathin, defect-free mMON nanofilms/membranes by separating organic units and metal linkers in two immiscible phases. As shown in Fig. 4a, a free standing TTSBI-Ti nanofilm was formed at the interface between two immiscible liquid phases with tetradecane as the solvent for $Ti(OBu)_4$ and NMP as the solvent for TTSBI, respectively. Fig. 4b shows the SEM image of a TTSBI-Ti nanofilm transferred onto an AAO support; the nanofilm was very smooth and no obvious pinholes and cracks were observed. This is consistent with the dye rejection results (see discussion below). Free standing HHTP-Ti nanofilm was also obtained following the same interfacial synthesis method (Fig. 4c and 4d).

TTSBI-Ti and HHTP-Ti membranes were deposited on porous AAO support by the interfacial synthesis process to investigate their separation performance for organic molecules. To provide sufficient mechanical strength and avoid the penetration of mMON nanofilms into the AAO support pores, a porous CNT network was deposited on the AAO support surface *via* vacuum filtration of pre-prepared CNT dispersion in water (see Fig. S12 for SEM images and Fig. S13 for the control experiment). A representative interfacial reaction process and structure of mMON membrane was shown in Fig. 5a. The CNT network supported by AAO was firstly fully soaked with NMP solution containing TTSBI or HHTP. After removing excess NMP solution by N_2 purging, tetradecane solution containing $Ti(OBu)_4$ was coated on the CNT network. After 2-min reaction at room temperature, mMON selective nanofilms/membranes were formed on the CNT network through controlled alcoholysis reaction at the NMP-tetradecane interface. The TTSBI-Ti membrane formed on the CNT network showed a dense and smooth surface (Fig. 5b). Cross-sectional SEM image in Fig. 5b showed the thickness of TTSBI-Ti membrane formed by 2-min interfacial reaction between $Ti(OBu)_4$ (10 mM) in tetradecane and TTSBI (20 mM) in NMP was ~30 nm. HHTP-Ti membrane could also be formed by the same procedure (Fig. S14). Fig. 5c shows thickness of TTSBI-Ti membranes increased from 30, 60, 120 to 240 nm (refer to SEM images in Fig. S15) with the increasing precursor concentration. These membranes were denoted as TTSBI-Ti 30-nm, TTSBI-Ti 60-nm, TTSBI-Ti 120-nm and TTSBI-Ti 240-nm.

OSN performance

mMON nanofilms/membranes were evaluated for OSN application owing to their high chemical stability and molecular-sized micropores. As shown in Fig. 6a, for TTSBI-Ti membrane with thickness of 30 nm, methanol permeance was

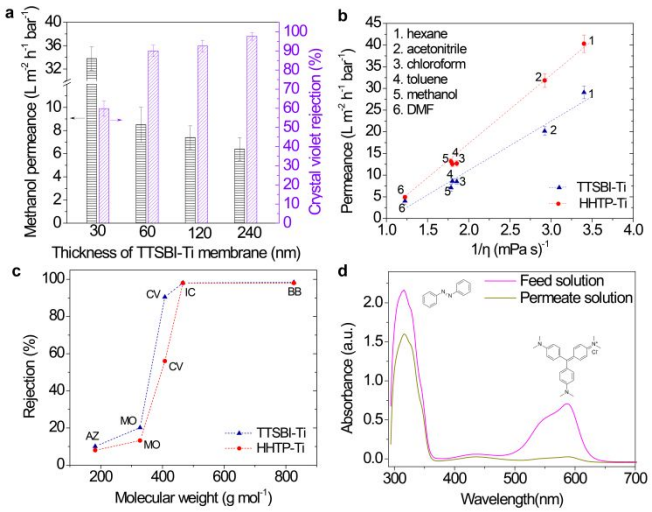

Fig. 6 Organic solvent nanofiltration and molecular separation performance. **a**, Methanol permeance and CV rejection of TTSBI-Ti membranes with different thickness. **b**, Permeance of pure organic solvents through TTSBI-Ti 60-nm and HHTP-Ti 60-nm membranes. **c**, Rejection of selected dyes in methanol versus their molecular weight. The dyes used: AZ, MO, CV, IC and BB. **d**, UV-vis absorbance spectra of a mixture of AZ and CV solution before and after filtration through TTSBI-Ti 60-nm membrane.

up to 33.8 L m^{-2} h^{-1} bar^{-1}, but rejection for CV (molecular weight (MW): 408.0 g/mol) was only 60.0%, suggesting a loose structure and larger average pore size than CV molecule in such a thin membrane. When TTSBI-Ti membrane thickness increased to 60 nm, methanol permeance decreased to 8.5 L m^{-2} h^{-1} bar^{-1}, and rejection for CV increased to 90.1%, suggesting significantly narrowed membrane pores that were smaller than CV molecule. When membrane thickness further increased to 120 and 240 nm, methanol permeance decreased only slightly (12.9% and 24.7%, relative to methanol permeance of TTSBI-Ti 60-nm), with CV rejection increase to 92.5% and 97.6%. This is surprising, because when membrane thickness increased from 60 nm to 120 and 240 nm, methanol permeance would be expected to decrease by 2 and 4 times, if membrane structure were uniform. Apparently, TTSBI-Ti 60-nm, TTSBI-Ti 120-nm and TTSBI-Ti 240-nm have asymmetric structure. Only slightly lower methanol permeance and higher CV rejection of TTSBI-Ti 120-nm and TTSBI-Ti 240-nm than those of TTSBI-Ti 60-nm seem to suggest TTSBI-Ti 120-nm and TTSBI-Ti 240-nm have a denser bottom layer resulting in higher CV rejection but a looser top layer leading to low transport resistance. This asymmetric structure may result from the diffusion resistance of the pre-formed bottom mMON layer for metal linkers/organic units. We also adjusted $Ti(OBu)_4$ concentration in the preparation of TSBI-Ti membrane. As shown in Fig. S16, with the increase of the $Ti(OBu)_4$ concentration from 10 to 40 mM, CV rejection of the obtained TTSBI-Ti membranes increased from 61.4% to 97.4%. In the meantime, methanol permeance decreased from 19.2 to 6.7 L m^{-2} h^{-1} bar^{-1}, suggesting a denser membrane be formed at higher $Ti(OBu)_4$ concentration in the interfacial reaction process. Since TTSBI-Ti 60-nm demonstrated an acceptable compromise between permeance and rejection for CV molecule, further OSN evaluation was focused on this membrane. Permeance of organic solvents, including polar and nonpolar solvents (e.g. acetonitrile, chloroform, toluene, DMF, ethanol and hexane), through TTSBI-Ti 60-nm was measured. Fig. 6b shows the permeance of these solvents increased in inverse proportion to the viscosity. In case of the HHTP-Ti 60-nm, it showed a similar inverse proportionality between solvent permeance and viscosity. For membranes with microporous structure, viscous flow can be readily explained by Hagen-Poiseuille equation[48]. Generally, HHTP-Ti 60-nm exhibited higher organic solvent permeance than TTSBI-Ti 60-nm, probably because of its lager pore size (see BET results in Fig. S4b and S6b).

To evaluate the potential of mMON nanofilms/membranes for OSN, we performed dead-ended filtration tests with dye molecules of different MWs (molecular structures of dyes are shown in Tab. S2) using methanol as the solvent. Fig. 6c shows the dye rejection as a function of MW. TTSBI-Ti 60-nm showed low rejection for AZ (MW: 180.2 g/mol) and MO (MW: 327.3 g/mol), at 10.1% and 20.2%, respectively. For larger dyes, CV, IC (MW: 466.4 g/mol) and BB (MW: 826.0 g/mol), the rejection increased to 90.5%, 98.1% and 98.4%, respectively. These results suggest that MW cut off (MWCO) of TTSBI-Ti 60-nm was around 400 Dalton. For HHTP-Ti 60-nm, it also showed a low rejection for AZ (8.0%) and MO (13.2%) and high rejection for IC (98.2%) and BB (98.6%). A moderate rejection for CV was obtained for HHTP-Ti 60-nm, suggesting its MWCO was slightly larger than that of the TTSBI-Ti 60-nm, consistent with the results obtained from characterization of pore size using neutral solutes (Fig. S17). Tab. S3 presents OSN performance compared with previously reported membranes, the mMON membranes from this work also showed outstanding solvent permeance at the same selectivity. Furthermore, the surface charge property of the membranes was investigated via zeta potential measurement. As shown in Fig. S18, TTSBI-Ti membrane showed nearly neutral characteristic. Thus, in this OSN performance test, the interaction of solute charge with membrane surface charge is negligible. We infer that molecular-sized sieving plays the key role. To demonstrate precise molecular separation, TTSBI-Ti 60-nm was used to separate a binary dye mixture of AZ and CV (50% AZ/50%CV) with methanol as the solvent. Fig. 6d shows the UV-vis spectra of the feed and the permeate after filtration through TTSBI-Ti 60-nm. Clearly, after filtration, almost no CV molecules passed through the membrane, and AZ purity (relative to CV) reached as high as 94.0%. This clearly demonstrated a very sharp separation between these two dyes with molecular structure difference of approximately one aromatic ring by TTSBI-Ti 60-nm.

Conclusions

In summary, a new class of microporous metal-organic material, mMON, was designed and synthesized via alcoholysis reaction between contorted/rigid organic units with catechol groups and metal linkers. mMONs synthesized in this work exhibited similar microporosity to the existing microporous materials and high chemical stability in acidic solutions and various organic solvents. Design flexibility and desired features

of mMONs, combined with a compatible interfacial reaction process to form ultrathin membranes, endow mMONs with great potential for molecular separation by membrane technology.

Author Contributions

M.Y. and S.Z. conceived the idea and designed the research. S.Z., R.C. and H.L. performed experiments, including synthesis of materials and membranes, and characterization analysis. B.S. helped with the XRD and XPS test. G.B., R.Z. and S.L. provided suggestions and technical support. S.Z. and M.Y. wrote the manuscript. M.Y. guided the project. All the authors participated in the discussion and read the manuscript.

Conflicts of interest

There are no conflicts to declare.

Acknowledgements

We gratefully acknowledge the support by National Science Foundation (NSF) Career Award under Grant No. 1451887.

References

1. D. L. Gin and R. D. Noble, *Science*, 2011, **332**, 674-676.
2. P. Marchetti, M. F. Jimenez Solomon, G. Szekely and A. G. Livingston, *Chem. Rev.*, 2014, **114**, 10735-10806.
3. P. Bernardo, E. Drioli and G. Golemme, *Ind. Eng. Chem. Res.*, 2009, **48**, 4638-4663.
4. D. S. Sholl and R. P. Lively, *Nature*, 2016, **532**, 435-437.
5. H. B. Park, C. H. Jung, Y. M. Lee, A. J. Hill, S. J. Pas, S. T. Mudie, E. Van Wagner, B. D. Freeman and D. J. Cookson, *Science*, 2007, **318**, 254-258.
6. M. D. Guiver and Y. M. Lee, *Science*, 2013, **339**, 284-285.
7. Y. Peng, Y. Li, Y. Ban, H. Jin, W. Jiao, X. Liu and W. Yang, *Science*, 2014, **346**, 1356-1359.
8. H. Li, Z. Song, X. Zhang, Y. Huang, S. Li, Y. Mao, H. J. Ploehn, Y. Bao and M. Yu, *Science*, 2013, **342**, 95-98.
9. S. Karan, S. Samitsu, X. Peng, K. Kurashima and I. Ichinose, *Science*, 2012, **335**, 444-447.
10. S. Karan, Z. Jiang and A. G. Livingston, *Science*, 2015, **348**, 1347-1351.
11. Q. Yang, Y. Su, C. Chi, C. Cherian, K. Huang, V. Kravets, F. Wang, J. Zhang, A. Pratt and A. Grigorenko, *Nat. Mater.*, 2017, **16**, 1198-1202.
12. Z. Qiao, S. Zhao, M. Sheng, J. Wang, S. Wang, Z. Wang, C. Zhong and M. D. Guiver, *Nat. Mater.*, 2019, **18**, 163-168.
13. X. Guan, H. Li, Y. Ma, M. Xue, Q. Fang, Y. Yan, V. Valtchev and S. Qiu, *Nat. Chem.*, 2019, **11**, 587-594.
14. C.-N. Yeh, K. Raidongia, J. Shao, Q.-H. Yang and J. Huang, *Nat. Chem.*, 2015, **7**, 166.
15. L. Chen, G. Shi, J. Shen, B. Peng, B. Zhang, Y. Wang, F. Bian, J. Wang, D. Li and Z. Qian, *Nature*, 2017, **550**, 380-383.
16. H. Li, C. Qiu, S. Ren, Q. Dong, S. Zhang, F. Zhou, X. Liang, J. Wang, S. Li and M. Yu, *Science*, 2020, **367**, 667-671.
17. M. Y. Jeon, D. Kim, P. Kumar, P. S. Lee, N. Rangnekar, P. Bai, M. Shete, B. Elyassi, H. S. Lee and K. Narasimharao, *Nature*, 2017, **543**, 690-694.
18. X. Xu, W. Yang, J. Liu and L. Lin, *Adv. Mater.*, 2000, **12**, 195-198.
19. Y. S. Li, H. Bux, A. Feldhoff, G. L. Li, W. S. Yang and J. Caro, *Adv. Mater.*, 2010, **22**, 3322-3326.
20. H. Guo, G. Zhu, I. J. Hewitt and S. Qiu, *J. Am. Chem. Soc.*, 2009, **131**, 1646-1647.
21. M. S. Denny, J. C. Moreton, L. Benz and S. M. Cohen, *Nat. Rev. Mater.*, 2016, **1**, 1-17.
22. A. P. Cote, A. I. Benin, N. W. Ockwig, M. O'Keeffe, A. J. Matzger and O. M. Yaghi, *Science*, 2005, **310**, 1166-1170.
23. J. Jiang, Y. Zhao and O. M. Yaghi, *J. Am. Chem. Soc.,* 2016, **138**, 3255-3265.
24. S. Yuan, X. Li, J. Zhu, G. Zhang, P. Van Puyvelde and B. Van der Bruggen, *Chem. Soc. Rev.*, 2019, **48**, 2665-2681.
25. C. Fan, H. Geng, H. Wu, Q. Peng, X. Wang, B. Shi, Y. Kong, Z. Yin, Y. Liu and Z. Jiang, *J. Mater. Chem. A,* 2021*, **9,*** 17720-17723.
26. M. Pera-Titus, *Chemical reviews*, 2014, **114**, 1413-1492.
27. A. Huang, Q. Liu, N. Wang, Y. Zhu and J. r. Caro, *J. Am. Chem. Soc.*, 2014, **136**, 14686-14689.
28. A. J. Brown, N. A. Brunelli, K. Eum, F. Rashidi, J. Johnson, W. J. Koros, C. W. Jones and S. Nair, *Science*, 2014, **345**, 72-75.
29. L. Sheng, C. Wang, F. Yang, L. Xiang, X. Huang, J. Yu, L. Zhang, Y. Pan and Y. Li, *Chem. Commun.*, 2017, **53**, 7760-7763.
30. Y. Wang, H. Jin, Q. Ma, K. Mo, H. Mao, A. Feldhoff, X. Cao, Y. Li, F. Pan and Z. Jiang, *Angew. Chem. Int. Ed.*, 2020, **59**, 4365-4369.
31. S. Zhang, Z. Wang, H. Ren, F. Zhang and J. Jin, *J. Mater. Chem. A,* 2017, **5***,* 1962-1966.
32. X. Ma, P. Kumar, N. Mittal, A. Khlyustova, P. Daoutidis, K. A. Mkhoyan and M. Tsapatsis, *Science*, 2018, **361**, 1008-1011.
33. Z. Lai, G. Bonilla, I. Diaz, J. G. Nery, K. Sujaoti, M. A. Amat, E. Kokkoli, O. Terasaki, R. W. Thompson and M. Tsapatsis, *Science*, 2003, **300**, 456-460.
34. M. Carta, R. Malpass-Evans, M. Croad, Y. Rogan, J. C. Jansen, P. Bernardo, F. Bazzarelli and N. B. McKeown, *Science*, 2013, **339**, 303-307.
35. N. B. McKeown and P. M. Budd, *Chem. Soc. Rev.*, 2006, **35**, 675-683.
36. L. D. Nghiem, P. Mornane, I. D. Potter, J. M. Perera, R. W. Cattrall and S. D. Kolev, *J. Membr. Sci.*, 2006, **281**, 7-41.
37. N. Du, H. B. Park, G. P. Robertson, M. M. Dal-Cin, T. Visser, L. Scoles and M. D. Guiver, *Nature materials*, 2011, **10**, 372-375.
38. B. S. Ghanem, R. Swaidan, E. Litwiller and I. Pinnau, *Adv. Mater.*, 2014, **26**, 3688-3692.
39. J. R. Wiegand, Z. P. Smith, Q. Liu, C. T. Patterson, B. D. Freeman and R. Guo, *J. Mater. Chem. A*, 2014, **2**, 13309-13320.
40. P. Gorgojo, S. Karan, H. C. Wong, M. F. Jimenez‐Solomon, J. T. Cabral and A. G. Livingston, *Adv. Func. Mater.*, 2014, **24**, 4729-4737.
41. P. M. Budd and N. B. McKeown, *Polym. Chem.*, 2010, **1**, 63-68.
42. S. Tsarkov, V. Khotimskiy, P. M. Budd, V. Volkov, J. Kukushkina and A. Volkov, *J. Membr. Sci.*, 2012, **423**, 65-72.
43. M. F. Jimenez-Solomon, Q. Song, K. E. Jelfs, M. Munoz-Ibanez and A. G. Livingston, *Nat. Mater.*, 2016, **15**, 760-767.
44. P. Sarkar, S. Modak and S. Karan, *Adv. Funct. Mater.* 2021, **31**, 2007054.

45. K. Tiwari, P. Sarkar, S. Modak, H. Singh, S. K. Pramanik, S. Karan and A. Das, *Adv. Mater.* 2020, **32**, 1905621.
46. P. Sarkar, S. Modak, S. Ray, V. Adupa, K. A. Reddy and S. Karan, *J. Mater. Chem. A*, 2021, **9**, 20714-20724.
47. M. C. Biesinger, L. W. Lau, A. R. Gerson and R. S. C. Smart, *Appl. Surf. Sci.*, 2010, **257**, 887-898.
48. B. R. Byron, S. Warren E. and L. Edwin N., *Transport Phenomena, Second Revised Edition*, John Wiley & Sons, New York, 2007 pp: 66-74.